This is a preprint, the final version is subject to change, of the American Mineralogist (MSA)
Cite as Authors (Year) Title. American Mineralogist, in press.
DOI: https://doi.org/10.2138/am-2019-6899

Manuscript 6899 – Revision 2 (Corrections on 25/06/19)

The Italian Solfatara as an analog for Mars fumarolic alteration

Flahaut Jessica[1*], Janice L. Bishop[2], Simone Silvestro[2,3], Dario Tedesco[4], Isabelle Daniel[5] and Damien Loizeau[6]

1- Centre de Recherches Pétrographiques et Géochimiques (CRPG), UMR7358 CNRS-Université de Lorraine, 15 rue Notre-Dame des Pauvres, 54500 Vandœuvre-lès-Nancy, France.
2- Carl Sagan Center, The SETI Institute, Mountain View, CA 94043, USA.
3- INAF- Osservatorio Astronomico di Capodimonte, Napoli, Italy.
4- Campania University - Luigi Vanvitelli, Caserta, Italy.
5- Université de Lyon, Université Lyon 1, Ens de Lyon, CNRS, UMR 5276, Lab. de Géologie de Lyon, Villeurbanne F-69622, France.
6- IAS, CNRS/Université Paris Sud, 91400 Orsay, France.

*Corresponding author: Dr Jessica Flahaut, Centre de Recherches Pétrographiques et Géochimiques, 15 rue Notre-Dame des Pauvres, 54500 Vandœuvre-lès-Nancy, France. Email : jessica.flahaut@univ-lorraine.fr

Keywords

Mars analog, hydrothermalism, vents, fumaroles, alteration patterns, Solfatara, VNIR spectroscopy, Raman spectroscopy, XRD

Abstract

This is a preprint, the final version is subject to change, of the American Mineralogist (MSA)
Cite as Authors (Year) Title. American Mineralogist, in press.
DOI: https://doi.org/10.2138/am-2019-6899

The first definitive evidence for continental vents on Mars is the *in situ* detection of amorphous silica-rich outcrops by the Mars Exploration Rover Spirit. These outcrops have been tentatively interpreted as the result of either acid sulfate leaching in fumarolic environments or direct precipitation from hot springs. Such environments represent prime targets for upcoming astrobiology missions, but remain difficult to identify with certainty, especially from orbit. In order to contribute to the identification of fumaroles and hot spring deposits on Mars, we surveyed their characteristics at the analog site of the Solfatara volcanic crater in central Italy. Several techniques of mineral identification (VNIR spectroscopy, Raman spectroscopy, XRD) were used both in the field, and in the laboratory on selected samples. The faulted crater walls showed evidence of acid leaching and alteration into the advanced argillic-alunitic facies, with colorful deposits containing alunite, jarosite and/or hematite. Sublimates containing a variety of Al and Fe hydroxyl-sulfates were observed around the active fumarole vents at 90°C. One vent at 160°C was characterized by different sublimates enriched in As and Hb sulfide species. Amorphous silica and alunite assemblages that are diagnostic of silicic alteration were also observed at the Fangaia mud pots inside the crater. A wide range of minerals was identified at the 665 m diameter Solfatara crater that is diagnostic of acid-steam heated alteration of a trachytic, porous bedrock. Importantly, this mineral diversity was captured at each site investigated with at least one of the techniques used, which lends confidence for the recognition of similar environments with the next generation Mars rovers.

Introduction

Hydrothermal systems have often been proposed as a possible cradle for early life (e.g., Shock, 1996; Nisbet and Sleep, 2001) and therefore represent a prime astrobiology target. Hydrothermal environments have long been presumed to exist on Mars based on orbital observations, terrestrial

analogs, and martian meteorites (e.g., Farmer et al., 1996; Ruff et al., 2011; Carr and Head, 2010). Evidence for warm and wet environments include the orbital detections by recent VNIR spectral-imagers of a wide range of hydrated minerals (Bibring et al., 2006; Murchie et al., 2009, Carter et al., 2013). In particular, the detection of chlorite, prehnite, epidote, serpentine and carbonates evidences aqueous alteration of Mars basaltic crust at high temperatures (e.g., Murchie et al., 2009; Ehlmann et al., 2009; Carter et al., 2013). Alteration by hydrothermal circulation in the cooling crust and impact-generated hydrothermal alteration have both been proposed as a plausible formation mechanism (e.g., Abramov and Kring, 2005; Carter et al., 2010, 2013; Ehlmann et al., 2009, 2011; Carr and Head, 2010). Hydrothermalism is also invoked as a likely source for alteration in localized surface environments (fumarolic fields or hot springs), leading to the formation of the clays, sulfates and silica-rich deposits identified in Valles Marineris Chasma (Milliken et al., 2008; Thollot et al., 2012), the silica detections in the Nili Patera caldera (Skok et al., 2010) or the serpentine and Mg-carbonate detections in Nili Fossae (Viviano et al., 2013). However, the first definitive evidence for volcanic hydrothermal activity (continental vents) on Mars is the *in situ* detection of amorphous silica-rich outcrops (>90% wt opal-A) by the Mars Exploration Rover (MER) Spirit Miniature Thermal Emission Spectrometer (Mini-TES) instrument (Squyres et al., 2008). The detection of abundant opaline silica at Home Plate, combined with high Ti content in local soils, was interpreted as an evidence for the dissolution of basaltic soils by low pH fluids (Squyres et al., 2008). Iron and phosphate-rich soils detected nearby, at Paso Robles, were also interpreted as acid-sulfate alteration products in a hydrothermal (possibly fumarolic) environment of primary phosphate-rich materials (Hausrath et al., 2013). The nodular aspect of the Home Plate outcrops led to an alternative suggestion that the Gusev silica could originate from the direct precipitation of sinters as observed in terrestrial hot springs (Ruff et al., 2011, 2014; Ruff and Farmer, 2016). The objective of this study is to

characterize in detail the fumarolic environments (and alteration patterns) at the Solfatara as a Mars analog site (Campi Flegrei, Italy), and discuss the possibilities and limits of identifying them on Mars. This specific analog site is used to show how trachytic rocks at the volcanic crater were hydrothermally altered into sulfate and silica-rich assemblages. Nevertheless, a variety of alteration assemblages can be produced via fumarolic alteration depending on several factors (e.g., composition of the bedrock, composition of the fluids). Therefore, the Solfatara site may be analogous to a some martian hydrothermal environments, which are likely to be more diverse.

Geologic setting

The Solfatara volcano is the most active site of the Campi Flegrei (CF) caldera, a quaternary volcanic complex located north of the city of Naples, in the Campanian plain graben (Figure 1). Straddling between the Tyrrhenian Sea to the west and the Apennines to the east, the Campanian plain is thought to originate from the stretching and thinning of the continental crust in an extensional back-arc context. The Campanian plain region is characterized by a general tensional NE-SW and NW-SE tectonic regime, and upwards migrations of magma that resulted in large ignimbrite eruptions starting from 290,000 years ago (e.g., Torrente et al., 2010). The largest of the Campanian plain volcano, Campi Flegrei (CF), is a 12km wide, partly submerged depression, inherited from two major collapses during the Campanian Ignimbrite eruption 37,000 years ago and the Neapolitan Yellow Tuff eruption 12,000 years ago (e.g., Rosi et al., 1983; Piochi et al., 2014 and references therein). The area was later affected by numerous large explosive eruptions that resulted in the formation of more than 20 craters including the 665 m wide, 4200 year old Solfatara volcanic crater (e.g., Armienti et al., 1983; Rosi and Sbrana, 1987; Di Vito et al., 1999; Pappalardo et al., 2002; Piochi et al., 2014; Isaia et al., 2015). The CF volcanic complex of potassic alkaline affinity is filled with km-thick pyroclastic deposits, overlapping Miocene flysch

facies terrains and Triassic-Paleocene carbonatic outcrops (e.g., Cameli et al., 1975). Previous analyses at the CF Solfatara reported the presence of incoherent products and ignimbrites of trachyte to trachyandesite composition, in addition to localized alteration (e.g., Rosi et al., 1983). Current volcanic activity in the CF is expressed through fumarole emissions, thermal pools and passive soil degassing that are most active within the Solfatara crater. According to geophysical measurements, the CF area is underlain by a magma reservoir located at 5 km depth and a Moho interface at 7 - 25 km depth (Ferrucci et al., 1989; Brandmayr et al., 2010). Combined with recent eruptive activity, this shallow mantle occurrence results in a local high heat flux of up to 200 $mW.m^{-2}$ (Piochi et al., 2014, and references therein). Shallow intrusions and degassing of magma drive unrest at the Phlegraean fields, and bradyseismic events are frequent in the Pozzuoli area, where the Solfatara crater is located (Tedesco, 1994; Caliro et al., 2007; Piochi et al., 2014).

Currently the Solfatara area is one of the most active fumarolic manifestations worldwide, with a diffuse degassing CO_2 rate > 1500 $ton.day^{-1}$ (Caliro et al., 2007, 2014 and reference therein). Gas emissions at the Solfatara include H_2O and CO_2 with H_2S, N_2, H_2, CH_4, He, Ar, and CO as a minor species (e.g., Chiodini et al., 2001; Caliro et al., 2007). Fumaroles are distributed along the crater NE and SE faulted rims, whereas mud pots occupy its central region (Figure 1). Stable isotope analyses of the water suggested that the Solfatara fumarolic discharge results from a mixture of CO_2-rich fluids degassed from a magma body and the vapor generated at 360°C from hydrothermal fluids (Caliro et al., 2007). Underground temperatures between 200 and 300°C were estimated from the mixed rising plume, using geochemical modeling (e.g., Tedesco and Sabroux, 1987, Tedesco et al., 1988). Furthermore, S isotopic compositions of H_2S from fumaroles argue for a typical magmatic origin (Allard et al., 1991), while epithermal minerals support the formation of sulfur species by acidic interaction of H_2S with the host rock via

119 oxidation to H_2SO_4, in a steam-heated environment (e.g., Valentino et al., 1999; Piochi et al.,
120 2015).
121
122 **Sample collection and analyses**
123 Alteration patterns at and around the mud pots (locally named Fangaia) and fumaroles were
124 studied with portable Visible Near InfraRed (VNIR) and Raman spectrometers at 7 sites within
125 the crater during a field campaign in September, 2015 (Figure 1c). Rock samples were collected
126 for laboratory characterization by X-Ray Diffraction (XRD) and chemical analyses (Tables 1-4;
127 Figures 1c and 2; Flahaut et al., 2017a).
128 VNIR reflectance spectra were measured onsite with an Analytical Spectral Devices (ASDinc)
129 field spectrometer. The ASDinc Fieldspec 4 Hi-Res instrument collects spectra in the 350 – 2500
130 nm domain (equivalent to 28000 – 4000 cm^{-1}) with a spectral resolution of 3 to 8 nm. All spectra
131 were acquired in the field with the contact probe (to limit the atmospheric contribution),
132 converted from radiance to reflectance using the ASDinc software and compared with the VNIR
133 spectra of reference minerals from the Bishop spectral library, as well as external sources such as
134 the USGS, RELAB, JPL and CRISM spectral libraries (e.g., Clark et al., 2007; Murchie et al.,
135 2007; Kokaly et al., 2017).
136 Raman spectra were also measured onsite with a portable Raport instrument from the LGL-TPE
137 (Lyon, France). Using a 532 nm - 30 mW laser source, the instrument has a sampling resolution
138 of 4-6 cm^{-1} between 100 cm^{-1} and 4000 cm^{-1}. However, given the large amount of amorphous
139 material within the crater, few diagnostic signatures were observed *in situ*. Additional Raman
140 spectra were collected on specific samples or grains at the LGL-TPE laboratory using an Xplora
141 Raman instrument coupled to an Olympus BX41 microscope and a at 532 nm laser source.

Spectra were compared with the reference Raman spectra of minerals in the RUFF libraries and WURM database (Downs and Hall-Wallace, 2003; Caracas et al., 2011).

Semi-quantitative X-Ray diffraction was performed using a Bruker D8 Advance diffractometer equipped with a Cu X-ray source at the Centre de Diffractométrie of the University Lyon 1, France. Samples were dried at 70°C for 48 hours, ground in an agate mortar, and dry sieved to <100 μm prior to measurement. A possible caveat of this preparation in the laboratory is that the phases detected are those observed in ambient laboratory conditions and may not reflect the hydration/structural state of these phases *in situ.* Random powder measurements were made over a 2-theta range of 3° to 70º. Oriented measurements were also performed on selected samples to enhance the signal originating from the (001) plane of potential clays, but none were detected. XRD patterns were analyzed and interpreted using the Bruker DIFFRAC. SUITE EVA software, and the fits were performed by comparing the d-spacing values to those in minerals of the International Center for Diffraction Data database and the Crystallography Open Database (Kabekkodu et al., 2002; Grazulis et al., 2009). The identity and relative mineral abundances were derived from the analyses, using corundum as an external standard. Mineral abundances are expressed as weight percent (wt. %) of mineral species with ~ 5 % accuracy. The degree of crystallinity, DOC, is also calculated from the total areas under the defined crystalline and amorphous components (Table 3).

In addition, major element analyses by ICP-OES, selected trace element analyses by ICP-MS, and S analyses were subcontracted for a selection of rock powder samples (amorphous material of the mud pots and fresher samples from crater walls) at the SARM facility in Nancy, France (Tables 2 and 4).

This is a preprint, the final version is subject to change, of the American Mineralogist (MSA)
Cite as Authors (Year) Title. American Mineralogist, in press.
DOI: https://doi.org/10.2138/am-2019-6899

Results

Nature of the bedrock in the crater walls

The local bedrock at Solfatara is comprised of incoherent ignimbrites (pyroclastic fallout, pyroclastic density currents, coarse to fine ash beds) as exposed in the crater walls (e.g., at site L3, Figure 2d), originating from the third and latest subaerial Campanian eruptive period ~ 4500 years ago (Isaia et al., 2015). With a Si content > 80 wt% and total alkali content of ~0.2-0.3 wt% (Table 2), samples L5R4, L3R1 and L6R1 from the relatively unaltered crater walls plot well in the field of rhyolite in a TAS (Total Alkali vs Silica) diagram. However, it is difficult to find pristine bedrock samples; high Si and Ti concentrations and elevated chemical index of alteration (CIA) indices in these apparently "fresh" ignimbrites suggest that they have been exposed to several episodes of leaching (Table 2). From a mineralogical point of view, all of samples L5R4, L3R1 and L6R1 have a more porous / ashy texture, and are mostly dominated by amorphous Si-rich material (> 90 wt%) with minor amounts of anatase (TiO_2) and calcite ($CaCO_3$) (Table 3). More rocky wall samples such as L6R3 and L6R5 are composed of > 85 wt% of the alkali feldspar sanidine ($KAlSi_3O_8$) and correspond to trachytic compositions. Native sulfur was not detected in the bedrock samples by XRD, but bulk chemical analyses reveal S contents between 0.3 and 1.4 wt%.

The bedrock material does not show specific Raman or VNIR spectral signature; weak hydration bands are observed in some outcrops (Figure 3a, black spectrum; Flahaut et al., 2017a). The rather symmetric shape of the 1.9 μm band, coupled with the lack of specific Raman signatures, suggests the presence of a hydrated amorphous sulfate, although hydrated silica could also be a possible interpretation (Figure 3a). The rounded spectral features near 1.42, 1.91, and 2.23 μm

188 observed for sample L6R1 are strikingly similar to those in opal spectra (C1JB874, McKeown et
189 al., 2011).
190 Yellow to orange coatings cover the walls locally, which suggests that alteration by sulfur-rich
191 fumarolic gases occurred as they reached the surface and condensed over the porous ignimbrites
192 (sites L2, L3, L6; Figure 2c, d, h, k). Limited outcrops also show dark red (e.g., L6R5, L6R10),
193 grey or turquoise-green colors (e.g., L5R4, L6R6) (Flahaut et al., 2017a). Colorful coatings were
194 abundant along the NE and SE faulted crater walls, where the fluid circulation might be more
195 intense. The paucity of vegetation within the crater defines an area of diffuse degassing much
196 larger than the fumarolic vents and faulted areas. At site L6, a whitish zone delineates a valley
197 cutting the crater rim and the weathered colored wall, suggesting recent erosion and dissolution
198 by rainfall and surficial water runoff (Figure 2k). As sites L2 and L3 are similar to L6 but with a
199 limited extent and a greater vegetation cover, samples from these sites were not analyzed by
200 XRD and ICP-OES.
201 VNIR spectra of samples from sites L2, L3, L6R1 to R10 are consistent with alunite
202 $KAl_3(SO_4)_2(OH)_6$, jarosite $KFe_3^{3+}(SO_4)_2(OH)_6$ and hematite Fe_2O_3 (Figure 3a). Alunite is
203 identified by features near 1.48, 1.76, and 2.16, 2.31 μm and jarosite by features near 0.92, 1.47,
204 1.85, and 2.26 μm (Bishop and Murad, 2005). The VNIR spectrum of hematite includes a
205 shoulder near 0.65 and a band near 0.85-0.88 μm that both vary in shape with grain size, but no
206 bands due to H_2O or OH (e.g. Morris et al., 1985, Morris and Lauer, 1990; Bishop and Murad,
207 2002). XRD analyses detect minor amount of jarosite, alunite, goldichite $KFe^{3+}(SO_4)_2 \cdot 4H_2O$,
208 alunogen $Al_2(SO_4)_3(H_2O)_{12}.5H_2O$ and carminite $Mg_7(SO_4)_5(OH)_4.H_2O$ (Figure 3), but no
209 hematite. This may indicate that the hematite observed by VNIR spectroscopy is poorly

crystalline. Raman spectra are consistent with the presence of sanidine remnants, anatase, alunite, jarosite and amorphous material (Figure 4a).

Sediments from the mud pots

CO_2 bubbles are continuously released from low temperature mud pools, or mud pots, located at the center of the crater (Site L1, fig. 1c, fig 2a,b). All three bubbling mud pots have a similar pH of ~1.5 and temperature of ~33°C (Flahaut et al., 2017a).

The shallow pools are filled with greyish, muddy deposits (L1R4). XRD analyses reveal the presence of ca. 50 % amorphous material consistent with opaline silica in agreement with the shape and position of the amorphous hump, and with the chemical analyses. Other components include ~ 25 wt% native sulfur and ~ 25 wt% alunite. Major element analyses confirmed the presence of a high abundance of volatile elements including sulfur (Table 4).

The pool ramparts are covered with silica coatings (L1R3Z1), whereas the muddy soil around the pool forms polygonal terrains during the dry season (L1R1), sometimes covered with a yellow coating (L1R2). XRD analyses show that the surrounding rocks contain less amorphous material than the pool material, and that the yellow deposits of sample L1R2 are primarily composed of alunogen + pickeringite ($MgAl_2(SO_4)_4 \cdot 22H_2O$), with minor K-alum and alunite. Clay minerals were not detected in the XRD patterns. All VNIR spectra are dominated by broad hydration features, consistent with amorphous silica (Figure 3b). The spectral bands are broadened to 1.41-1.48 and 2.16-2.21 μm and weak bands are present near 1.76 and 2.31 μm, all of which are consistent with a minor content of alunite. Raman spectra are consistent with the presence of native sulfur, sulfates and opal-A (broad bands at 310 and 780 cm^{-1}) (Figure 4b).

233 **Deposits from the fumarolic vents**

234 Material of various colors (white, yellow, orange and brown) and textures (fibers, needles,
235 bubbles…) with high crystalline contents (> 85% of the total phases) were collected from within
236 the vents at sites L5 and L6 at 90 °C (Fig. 2g, j; Flahaut et al., 2017a). VNIR analyses reveal the
237 presence of hydrated materials, likely including Al and Fe-rich sulfates (multiple absorptions
238 between 0.86-0.93 and 2.18-2.32 μm are observed; Figure 3c). Most spectra contain a strong
239 water absorption feature that dominates the spectra at wavelengths > 1.8 μm, which may indicate
240 the presence of highly hydrated sulfates such as alunogen or K-alum. However, no unique
241 spectral matches could be found in the reference libraries. This is likely also because of the
242 sensitivity of such hydrated phases to environmental conditions and their ability to adsorb water
243 near steam vents that is saturating their VNIR spectra. Samples R13 and R18 (site L6) show an
244 absorption band at 0.77 μm that is, coupled with features at 0.55, 1.48 and 1.97 μm, consistent
245 with coquimbite $Fe_2^{3+}(SO_4)_3 \cdot 9H_2O$. Orange-colored samples R15 and R19 have a diagnostic 0.87
246 μm iron absorption band similar to that of hematite, copiapite or ferricopiapite spectra. XRD
247 analyses revealed the presence of a variety of Al, K and Fe-sulfates (mostly alunogen, K-alum
248 $KAl(SO_4)_2 \cdot 12H_2O$, alunite, mercallite $KHSO_4$, goldichite, jarosite, coquimbite, plus traces of
249 yavapaiite $KFe(SO_4)_2$, millosevichite $Al_2(SO_4)_3$, tamarugite $NaAl(SO_4)_2 \cdot 6H_2O$, mixed with minor
250 Fe-oxides (e.g., ferryhydrite <2%)). Unfortunately, many of these minerals do not have matches
251 in the existing VNIR spectral libraries. These minerals are deposited in and around the vent
252 within ~1 m. These observations suggest that our samples correspond to fumarolic incrustations
253 and/or sublimated minerals; the former produced by gas cooling and condensation, while the
254 latter formed directly through vapor deposition processes (e.g., Africano and Bernard, 2000;
255 Aguilera et al., 2016).

A distinct variety of minerals was observed at the higher temperature vent at site L4 (gas emissions at 160°C, Figure 2e,f; Table 4). Realgar (AsS), Cinnabar (HgS) and Orpiment (As_2S_3) were identified thanks to their respective burgundy, red and yellow colors. These colorful minerals are only present as thin surficial coatings (sublimates), while the bulk of these rocks appear to be comprised of the same wall-rock as elsewhere. Spectra of these colorful minerals contain visible-region electronic absorptions corresponding to their colors, and they should not exhibit NIR spectral features since their structures do not include either H_2O, OH, or SO_4 (e.g., Cloutis et al., 2016). Cinnabar visible spectra are characterized by a steep absorption edge at 590 nm and no diagnostic absorption features longward of this edge to 2500 nm. Realgar and orpiment spectra are similar to that of cinnabar, but with absorption edges near shorter wavelengths, consistent with their more orange to yellow colors. Weak absorptions in the USGS library spectra of these minerals are attributed to adsorbed water. Strong VNIR OH and H_2O bands similar to those of silica sinters from the Yellowstone hot springs were observed in spectra of the L4 white samples, as well as bands near 2.03 and 2.16 μm in the L4 yellow samples, which may indicate the presence of amorphous As_2S_3, and hydrated amorphous FeAs species (Figure 3d; Bishop et al., 2004a; Henke, 2009). Raman spectra also lack references for comparison but are consistent with As-bearing species (Figure 4c). XRD or ICP-OES / ICP-MS analyses were not be performed due to the potential toxicity of the samples.

Discussion

Mineralogical detections and alteration

A large variety of minerals have been detected in the Solfatara crater samples, in agreement with previous studies (e.g., Sgavetti et al., 2009; Valentino et al., 1999). Remnants of sanidine in some wall samples are consistent with the presumed, original trachytic composition of the rock. Less

competent ash layers are consistent with a high proportion of amorphous material. Calcite detections in the wall samples at L3 and L5 could originate from the underlying sedimentary rocks, or have precipitated as a secondary mineral. Elevated Si and Ti concentrations suggest leaching processes and alteration within the entire crater.

Silicic alteration around mud pots in the central part of the crater is characterized by the complete destruction of the original rock/ primary mineral assemblage as evidenced in the XRD patterns of site L1 samples. The product of this alteration is a porous rock consisting exclusively of residual amorphous silica associated with sulfur and alunite. Secondary minerals such as K-alum, alunogen and pickeringite are detected in the dry, surrounding deposits, a few meters away from the pools (sample L1R2). No phyllosilicates were detected in the L1 (active) mud pots; the low pH likely hindering the formation of kaolinite (Zimbelman et al., 2005). Muddy gray material in the pools is consistent with amorphous silica. However, small absorption bands in the VNIR spectra of L7 (dry, ancient mud pot towards the periphery of the crater) suggest the presence of minor Al-clays such as kaolinite or montmorillonite (figure 3b). Alunite formation from K – feldspar hydrolysis has been confirmed by previous SEM and isotopic analyses (Piochi et al., 2015; Mayer et al., 2016). Alunite dominance in the mud pot samples L1R3 and L1R4 could also result from the hydrolysis of the K-alum of sample L1R2 in the low pH, wet pool environment (Valentino et al., 1999).

Along the crater rim (sites L2, L3, L6), alteration shifts towards the so-called “advanced argillic (or alunitic) facies”. The original rocks are replaced by minerals of the alunite group, natroalunite, alunite and jarosite with a prevalence of alunite. These observations are consistent with the sequential zoning observed at several volcanoes, and could be explained by progressive neutralization of the fluid away from the degassing vents (e.g., Fulignati et al., 1998). The spatial distribution of alunite and jarosite at sites L2, L3 and L6 could be related to the relative

availability of Fe and Al within the bedrock. At a temperature close to 100°C (most gas emissions at Solfatara), alunite and jarosite share a stability boundary at low pH, while at higher pH alunite is presumably associated with hematite (Zimbelman et al., 2005). We observed both mineral assemblages in some rocks of site L6. VNIR spectra of the L6 alunite-bearing rock (L6R4) share common absorption features with K-alunite references at 1.43 and 1.48 μm (rather than 1.44 and 1.49 μm for Na-alunite), indicating that this sample contains K-alunite (Figure 5a). The shape of the 2.22/2.26 μm doublet feature in the jarosite spectra from the Solfatara outcrops are also more consistent with the K-rich endmember, in agreement with the original bedrock composition (Figure 5b). The spectrum of sample L2R1 includes VNIR features consistent with the presence of both alunite and jarosite.

Jarosite is expected to form at low pH ~2-4 (e.g. Bigham et al., 1996; Elwood Madden et al., 2004), which would be inconsistent with the preservation of K-feldspar. Still, both are observed in the same area, suggesting that alteration is concentrated in layers that are more porous, or fractured and is spatially highly variable. The assemblage silica + alunite ± jarosite is diagnostic of advanced clay alteration as produced by acidic fluids in a steam-heated environment, in the upper portion of hydrothermal systems (Rye, 2005) such as solfataras (e.g., Bishop et al., 2007). Previous isotopic measurements of ^{34}S in sulfate minerals and native sulfur and H_2S in the fumarolic gases tend to confirm that the sulfates originate from the oxidation of H_2S. While it seems clear that sulfur and sulfates are mostly derived from the H_2S-gas (Allard et al., 1991), the debate is still vivid regarding the high versus low sulfidation grade of the CF system, and especially in the Solfatara area, given that the observed mineralization could be derived from either one or the other or both processes (e.g., Rye, 2005; Piochi et al., 2015). Recent petrological and isotopic surveys concluded that the CF is consistent with a low sulfidation system that may

transition towards a high sulfidation system in the most active centers (e.g., Solfatara) (Piochi et al., 2015).

A wide variety of sulfate minerals is also detected in the direct vicinity of active fumarole vents. Crystalline Al and Fe hydroxysulfates are detected in areas where the bedrock lacks indication of primary sulfides, suggesting the influence of fumarole deposits and consistent with a steam-heated environment. Sublimates include alunite, alunogen, alum K, mercallite, goldichite, coquimbite, ferrihydrite, millosevichite and tamarugite, which are highly soluble minerals not often preserved. At the highest temperature vent (site L4), sublimates form coatings bearing various arsenic and mercury species, generally found in epithermal systems. Orpiment and other arsenic sulfide minerals are likely derived from the oxidation of realgar.

Coordination of measurement techniques

VNIR, Raman and XRD analyses were carried out to determine the mineralogy of the samples. The results of these techniques are generally in good agreement (Table 5), but VNIR and Raman surveys can be swayed by coatings (e.g., hematite at site L6, arsenic bearing species) as their sensitivity is limited to the first few top μm of the surface. VNIR and Raman techniques are advantageous in that they are fast, non-destructive, and do not require sample preparation. XRD analyses are however useful in gaining insights into minerals that are easily masked or have no signatures in the VNIR (e.g., feldspars, quartz), and mandatory for deriving quantitative information. The XRD technique is also the sole one to provide access to the full mineral assemblage in the case of complex mixtures, whilst VNIR and Raman measurements often reveal only a few phases.

Most sulfates could easily be identified with all of these individual techniques, although Raman and VNIR reference libraries do not necessarily contain all of the minerals identified by XRD.

Some anhydrous sulfates such as yavapaiite do not exhibit spectral features in the NIR (e.g. Lane et al., 2015). Some sulfate species (e.g., tamarugite) could only be recognized thanks to the vast, historical XRD standard database. Similarly, the existing VNIR and Raman databases lacked exact matches for all the arsenic sulfides and iron-bearing species that seemed to be derived from, or associated with realgar. Amorphous silica detection is not as straightforward as sulfate detection, but its presence could be inferred in the VNIR data, that are in general more efficient at characterizing hydrated amorphous components than Raman and XRD. Alternatively, the presence of amorphous silica can be inferred from the combined chemical analyses and XRD results. A suite of complementary techniques, such as the one described above, presents the most effective procedure to derive the most comprehensive information on hydrothermal samples in the field.

Both VNIR and Raman spectrometers will be carried onboard the next generation Mars rovers (e.g., MicrOmega on ExoMars (Bibring et al., 2017), ISEM on ExoMars (Korablev et al., 2017), RLS on ExoMars (Rull et al., 2017), SuperCam on Mars2020 (Wiens et al., 2016), SHERLOC on Mars2020 (e.g., Beegle et al., 2014)). A key advantage of both techniques is their efficiency, as they can easily be deployed *in situ*, without requiring any sample preparation. A possible caveat will be the potential difference in the scale of analysis between the various instruments, at the grain scale for Raman, typically larger for VNIR spectrometers (with the exception of MicrOmega), as noted in previous analog studies (e.g., Flahaut et al., 2017b). Raman spectroscopy will, however, enable the possibility to identify minerals such as feldspar, anhydrous silicates or sulfates, and organic molecules, that are difficult to investigate in the VNIR domain (e.g. Bishop et al., 2003; Bishop and Murad, 2004; Lopez-Reyes et al., 2013; Sobron et al., 2014; Wiens et al., 2016; Flahaut et al., 2017b). VNIR spectroscopy will obviously

present great advantages to infer the presence of hydrated components, those containing Fe, OH, CO_3, SO_4, ClO_4, PO_4 etc., and distinguish between minerals of the same family (e.g., sulfates, see figure 4c). Together, these instruments will have a better chance to identify the key minerals at the selected landing sites. In the absence of XRD however, assessing the full petrologic assemblage of the outcrops or rock samples will only be possible through a combination of observations, e.g., elemental abundances from SuperCam, rock textures from ExoMars Close-UP Imager (CLUPI)... (e.g., Wiens et al., 2016, Josset et al., 2017).

Implications

VNIR spectroscopy is currently used on Mars as a remote sensing technique with instruments onboard spacecraft that map the planet's surface composition from a distance (e.g., the Observatoire pour la Minéralogie, l'Eau, les Glaces et l'Activité (OMEGA) instrument onboard Mars Express (Bibring et al., 2004), the Compact Reconnaissance Imaging Spectrometer for Mars (CRISM) instrument onboard Mars Reconnaissance Orbiter (Murchie et al., 2007)). Those instruments have the capacity to detect iron and hydrated minerals such as those described at the Solfatara analog site and should therefore be able to identify and map areas of silicic alteration (opaline silica + alunite, as seen in the Solfatara mud pots) and the sequential zoning into argillic-alunitic alteration (jarosite-alunite-hematite in the crater walls). Presumably, fumarolic sublimates and condensates (*e.g.,* Al/Fe hydroxyl-sulfates) are also detectable with VNIR spectroscopy techniques, but the main issue of Mars orbital instruments is their limited spatial resolution (18 m/pixel at best from CRISM). Mars VNIR hyperspectral imagers on lander/rover-based missions would have a greater chance of identifying active or former vents than orbital instruments that might only detect extended areas of alteration, e.g. large fumarolic fields or geothermal areas. A number of hydrated species, including amorphous hydrated silica and related

399 materials (e.g., Bishop et al., 2008; Milliken et al., 2008, Mustard et al., 2008; Skok et al., 2010;
400 McKeown et al., 2011; Wray et al., 2011; Weitz et al., 2013, 2014; Sun and Milliken, 2018) and
401 sporadic jarosite and alunite-rich outcrops (Swayze et al., 2008; Ehlmann et al., 2009, 2016;
402 Klingelhöfer et al., 2004; Morris et al., 2006; Farrand et al., 2009, 2014; Weitz et al., 2011;
403 Thollot et al., 2012; Michalski et al., 2013; Bishop et al., 2018), which could be of hydrothermal
404 origin, have been reported previously on Mars from orbital observations (Figure 6). Ongoing
405 efforts to understand the context of formation of those minerals, catalog their occurrences, and
406 recognize key alteration facies/assemblages are supported by analog studies.
407 More limited *in situ* observations already demonstrated the occurrence of hydrothermal processes
408 on Mars, although previous rovers were not equipped with VNIR or Raman spectrometers.
409 Amorphous silica was detected by the MER rover Spirit, at Home Plate, thanks to its mini-TES
410 thermal IR spectrometer. APXS chemistry indicated elevated Ti and P contents in nearby soils
411 that were interpreted as evidence for acid leaching; this process may have left behind some
412 alteration minerals. The presence of sulfates may be inferred in the TES wavelength range,
413 although hydrated minerals are most easily identified in the VNIR domain (e.g., Bibring et al.,
414 2006; Ehlmann et al., 2012) and are expected to be more readily observed by future rovers such
415 as ExoMars that include VNIR spectrometers. The presence of a VNIR or Raman spectrometer at
416 Gusev crater could help to further assess the presence of alteration minerals and possibly of
417 organics in areas where hydrothermal silica was detected by Spirit (Ruff et al., 2011; Ruff and
418 Farmer, 2016). Sending an XRD instrument to Gusev crater could bring additional information
419 on the nature and relative amount of crystalline phases in these unique silica-rich materials near
420 Home Plate (Ruff et al., 2011). The mini-TES instrument range was however well-suited for
421 capturing the mafic rock diversity in Gusev crater (e.g., Christensen et al., 2004). A significant
422 proportion of amorphous material has been detected at another Mars location, in the soils of Gale

Crater, by the CheMin XRD instrument on the Mars Science Laboratory rover. The nature and origin of this amorphous material could not be determined with certainty, but at least part of it seems to be hydrated (Bish et al., 2013; Dehouck et al., 2014; Achilles et al., 2017; Ehlmann et al., 2017; Yen et al., 2017; Rampe et al., 2018; Gabriel et al., 2018). As demonstrated above, VNIR spectroscopy was efficient as detected hydrated amorphous components such as opal, even in the pumice / ash component of the bedrock, and could assist in characterizing of the alteration phases identified by CheMin at Gale crater (e.g., Bish et al., 2013) if sent on future missions.

In the present study, we have shown an example of how trachytic rocks at the Solfatara crater were hydrothermally altered into sulfate and silica-rich assemblages. At the Solfatara site, steam-heated fumarolic alteration due to the presence of acidic sulfate-rich fluids resulted in an increased rock porosity and permeability, and the crater is currently primarily composed of incoherent rocks. The most abundant sulfates are Al, K, and Fe-rich in agreement with the original bedrock composition. Unlike the Solfatara site, the martian crust is more basaltic than trachytic (e.g., Mc Sween et al., 2003), even though trachytes and trachy-andesites have been found locally (e.g., Sautter et al., 2015; Cousin et al., 2017). Different alteration assemblages may be produced based on a number of factors that control hydrothermal alteration such as the rock type, but also the temperature, pressure, permeability, fluid composition and event duration (e.g., Browne, 1978). Previous Mars analog studies of andesitic basalt alteration in Nicaragua reported the presence of mixed phyllosilicates, oxides/hydroxides and sulfates (gypsum + alunite) in the active acidic volcanic systems of Cerro Negro, Momotombo, and Telica (Hynek et al., 2013; Marcucci et al., 2013). Acid-fog weathered basalts at the top of the Hawaian Kilauea volcano were found to be dominated by jarosite/natrojarosite sulfates, iron oxides and amorphous silica (e.g., Schiffman et al., 2006; Seelos et al., 2010). Icelandic expeditions have found abundant Al

and Fe/Mg smectites, hematite and hydrous silica, formed from the alteration of basalts by S-poor fluids (Ehlmann et al., 2012). All of these locations have presumed basaltic composition but show various assemblages due to varying external factors. Therefore, it is key to catalog in detail alteration patterns in these various environments and understand the geochemical pathways involved in those transformations on Earth, in order to shed light on past Mars environments.

A crucial aspect of hydrothermal systems is that on Earth, continental vents are known to be favorable to the development of life and the preservation of biosignatures. Therefore, they represent prime targets for the search of Life on Mars (e.g., Damer et al., 2017; Campbell et al., 2017). The Solfatara crater is home to several thermophilic, thermo-tolerant and acidophilic Bacteria, algae (e.g., *Cyanidium caldarium*) and Archea, such as *Sulfolobus solfataricus* (named after our study area, the Italian Solfatara), *Acidianus*, *Pyrobaculum* and *Metallosphaera sp* (e.g., DeRosa et al., 1974, 1975; Zillig et al., 1980; Huber et al., 2000a, b). Most of these micro-organisms are chemolithotrophs and rely on S, Fe oxides and metal sulfides for energy supply (e.g., Huber et al., 2000a, b). Finding such a biodiversity adapted to this extreme environment is promising for investigation of potential life elsewhere in the Solar System, and especially on Mars.

Acknowledgements

CTX and CRISM images of Mars were processed using the MarsSI web application (https://emars.univ-lyon1.fr/MarsSI/). Fieldwork was funded by a N.W.O. VENI grant to J. Flahaut. J. Flahaut was funded by two CNES ExoMars / LIS APR for sample analyses and by a Lorraine Université d'Excellence Future Leader grant at the time of writing / for publication fees. D. Loizeau received support from the European Research Council under the European Union's Seventh Framework Program (FP7/2007-2013)/ERC Grant agreement n° 280168. Support from

the NASA Astrobiology Institute and NASA's SSW program to J. Bishop is appreciated. The authors are very grateful to Dr. Giorgio Angarano, the Solfatara general manager for his strong support and help using and visiting each site of the crater. The authors also wish to thank the Lyon Raport team (G. Montagnac, R. Caracas, H. Cardon) for their help and instrument loan - the Raman facility in Lyon is supported by the Institut national des sciences de l'univers (CNRS). The authors would like to thank the CDHL at Université Lyon 1, and in particular Ruben Vera for his help with XRD. The authors are also grateful to the e-Mars Lyon team, especially Cathy Quantin-Nataf, and Patrick Thollot, for fruitful discussions. This is CRPG contribution N°2688.

References

Abramov, O. and Kring, D. A. (2005) Impact-induced hydrothermal activity on early Mars. Journal of Geophysical Research: Planets, 110(12), 1–19.

Achilles, C. N. et al. (2017) Mineralogy of an active eolian sediment from the Namib dune, Gale crater, Mars. Journal of Geophysical Research: Planets, 122(11), 2344-2361.

Africano, F. and Bernard, A. (2000) Acid alteration in the fumarolic environment of Usu volcano, Hokkaido, Japan. Journal of Volcanology and Geothermal Research, 97(1-4), 475-495.

Aguilera, F., Layana, S., Rodríguez-Díaz, A., González, C., Cortés, J., and Inostroza, M. (2016) Hydrothermal alteration, fumarolic deposits and fluids from Lastarria Volcanic Complex: A multidisciplinary study. Andean Geology, 43(2), 166-196.

Allard, P., Maiorani, A., Tedesco, D., Cortecci, G., Turi, B. (1991) Isotopic study of the origin of sulfur and carbon in Solfatara fumaroles, Campi Flegrei caldera. Journal of Volcanology and Geothermal Research, p. 139-159.

Armienti P, Barberi F, Bizojard H, Clocchiatti R, Innocenti F, Metrich N, Rosi M, Sbrana A (1983) The Phlegraean Fields: magma evolution within a shallow chamber. Journal of Volcanology and Geothermal Research, 17:289–311. doi:10.1016/0377-0273(83)90073-2.

Beegle, L. W. et al., (2014) SHERLOC: scanning habitable environments with Raman and luminescence for organics and chemicals, an investigation for 2020. In : AGU Fall Meeting Abstracts.

Bibring, J.-P. et al., (2004) OMEGA: Observatoire pour la minéralogie, l'eau, les glaces et l'activité, ESA-SP, p. 1240.

Bibring, J.-P. et al. (2006) Global mineralogical and aqueous mars history derived from OMEGA/Mars Express data. Science, 312(5772), 400–404.

Bibring, J.-P., Hamm V., Pilorget C., Vago J. L., MicrOmega Team (2017) The MicrOmega Investigation Onboard ExoMars. Astrobiology, Volume 17, Issue 6-7, pp.621-626. Doi: 10.1089/ast.2016.1642.

Bigham, J.M., Schwertmann U., and Pfab G. (1996) Influence of pH on mineral speciation in a bioreactor simulating acid mine drainage. Applied Geochemistry, 11, 845-849.

519

520 Bish, D. L. et al. (2013) X-ray diffraction results from Mars Science Laboratory: Mineralogy of
521 Rocknest at Gale crater. Science, 341(6153), 1238932.

522

523 Bishop, J.L. and Murad E. (2002) Spectroscopic and geochemical analyses of ferrihydrite from
524 springs in Iceland and applications to Mars. In J. L. Smellie and M. G. Chapman, Eds., Volcano-
525 Ice Interactions on Earth and Mars, 357-370. Geological Society, Special Publication No.202.
526 London.

527

528 Bishop, J. L., B. L. Anglen, L. M. Pratt, H. G. M. Edwards, D. J. Des Marais, and P. T. Doran
529 (2003) A spectroscopy and isotope study of sediments from the Antarctic Dry Valleys as analogs
530 for potential paleolakes on Mars, International Journal of Astrobiology, 2(4), 273-287.

531

532 Bishop, J. L., and E. Murad (2004) Characterization of minerals and biogeochemical markers on
533 Mars: A Raman and IR spectroscopy study of montmorillonite, Journal of Raman Spectroscopy,
534 35(6), 480-486.

535

536 Bishop, J. L., M. D. Dyar, M. D. Lane, and J. F. Banfield (2004a) Spectral identification of
537 hydrated sulfates on Mars and comparison with acidic environments on Earth, International
538 Journal of Astrobiology, 3(4), 275-285.

539

540 Bishop, J. L., Murad, E., Lane, M. D., and Mancinelli, R. L. (2004b) Multiple techniques for
541 mineral identification on Mars: a study of hydrothermal rocks as potential analogues for
542 astrobiology sites on Mars. Icarus, 169(2), 311-323.

Bishop, J. L., and E. Murad (2005) The visible and infrared spectral properties of jarosite and alunite, American Mineralogist, 90, 1100-1107.

Bishop, J.L., Schiffman, P., Murad, E., Dyar, M.D., Drief, A., and Lane, M.D., (2007) Characterization of alteration products in tephra from Haleakala, Maui: A visible-infrared spectroscopy, Mössbauer spectroscopy, XRD, EMPA and TEM study. Clays and Clay Minerals, 55(1), 1-17.

Bishop, J. L., E. Z. Noe Dobrea, N. K. McKeown, M. Parente, B. L. Ehlmann, J. R. Michalski, R. E. Milliken, F. Poulet, G. A. Swayze, J. F. Mustard, S. L. Murchie, and J.-. Bibring, P. (2008) Phyllosilicate diversity and past aqueous activity revealed at Mawrth Vallis, Mars, Science, 321(5890, 8 August 2008), doi: 10.1126/science.1159699, pp. 1159830-1159833.

Bishop, J. L., M. Parente, C. M. Weitz, E. Z. Noe Dobrea, L. A. Roach, S. L. Murchie, P. C. McGuire, N. K. McKeown, C. M. Rossi, A. J. Brown, W. M. Calvin, R. E. Milliken, and J. F. Mustard (2009) Mineralogy of Juventae Chasma: Sulfates in the Light-toned Mounds, Mafic Minerals in the Bedrock, and Hydrated Silica and Hydroxylated Ferric Sulfate on the Plateau, Journal of Geophysical Research, 114(E00D09), doi:10.1029/2009JE003352.

Bishop, J. L., J. J. Wray, A. M. Sessa, J. M. Danielson, B. L. Ehlmann, S. L. Murchie, B. Horgan, C. Gross, M. Parente, F. P. Seelos (2018) Evidence of Salty Residues in Layered Outcrops at Mawrth Vallis and Implications for Evaporative Environments on Early Mars. 49th Lunar and Planetary Science Conference, Abstract #1117.

Brandmayr, E, Raykova RB, Zuri M, Romanelli F, Doglioni C, Panza GF (2010) The lithosphere in Italy: structure and seismicity. In: Beltrando M, Peccerillo A, Mattei M, Conticelli S, Doglioni C (eds) The geology of Italy. Journal of the Virtual Explorer, Electronic edition ISSN 1441-8142, vol. 36, paper 1, doi:10.3809/jvirtex.2010.00224.

Browne, P.R.L. (1978) Hydrothermal alteration in active geothermal fields. Annual Review of Earth and Planetary Sciences, 6, 229-250.

Caliro, S., Chiodini, G., Moretti, R., Avino, R., Granieri, D., Russo, M., and Fiebig, J. (2007) The origin of the fumaroles of La Solfatara (Campi Flegrei, south Italy). Geochimica et Cosmochimica Acta, 71(12), 3040-3055.

Caliro, S., Chiodini, G., and Paonita, A. (2014) Geochemical evidences of magma dynamics at Campi Flegrei (Italy). Geochimica et Cosmochimica Acta, 132, 1-15.

Campbell, K. et al. (2017) Ubiquity, Diversity, and Preservation of Microbial Fabrics in Siliceous Hot Spring Deposits: Relevance to the Columbia Hills. The 3rd landing site workshop for the 2020 Mars Rover mission, Pasadena, CA.

Cameli, G.M., Puxeddu, M., Rendina, M., Rossi, A., Squarci, P., Taffi, L., (1975) Geothermal research in western Campania, southern Italy: geological and geophysical results. In: Proc. 2nd U.N. Symp. on Developement and Use of Geothermal Resources, San Francisco, Vol. 1, pp. 315–327.

Caracas, R. and Bobocioiu, E., (2011) The WURM project—a freely available web-based repository of computed physical data for minerals. American Mineralogist, 96(2-3), 437-443.

Carr, M. H. and Head, J. W. (2010) Geologic history of Mars. Earth and Planetary Science Letters, 294(3–4), 185–203. doi:10.1016/j.epsl.2009.06.042.

Carter, J., Poulet, F., Bibring, J.-P., and Murchie, S. L. (2010) Detection of hydrated silicates in crustal outcrops in the northern plains of Mars. Science, 328(5986), 1682–1686.

Carter, J., Poulet, F., Bibring, J. P., Mangold, N., and Murchie, S. L. (2013) Hydrous minerals on Mars as seen by the CRISM and OMEGA imaging spectrometers: Updated global view. Journal of Geophysical Research : Planets, 118(4), 831–858.

Chiodini, G., Frondini, F., Cardellini, C., Granieri, D., Marini, L., and Ventura, G., (2001) CO2 degassing and energy release at Solfatara volcano, Campi Flegrei, Italy. Journal of Geophysical Research: Solid Earth (1978–2012), 106(B8), 16213-16221.

Christensen, P. R. et al. (2004) Initial results from the Mini-TES experiment in Gusev Crater from the Spirit Rover. Science, 305(5685), 837-842.

Clark, R.N. et al. (2007) USGS Digital Spectral Library splib06a. U.S. Geological Survey, Digital Data Series, p. 231.

615 Cloutis, E. A., F. C. Hawthorne, S. A. Mertzman, K. Krenn, M. A. Craig, D. Marcino, M.
616 Methot, J. Strong, J. F. Mustard, D. L. Blaney, J. F. Bell, III, and F. Vilas (2006) Detection and
617 discrimination of sulfate minerals using reflectance spectroscopy, Icarus, 184, 121-157.
618
619 Cloutis, E., Norman, L., Cuddy, M., and Mann, P. (2016) Spectral Reflectance (350–2500 nm)
620 Properties of Historic Artists' Pigments. II. Red–Orange–Yellow Chromates, Jarosites, Organics,
621 Lead(–Tin) Oxides, Sulphides, Nitrites and Antimonates. Journal of Near Infrared Spectroscopy,
622 24(2), 119–140. doi:10.1255/jnirs.1207.
623
624 Cousin, A., Sautter, V., Payré, V., Forni, O., Mangold, N., Gasnault, O., Le Deit, L., Johnson, J.,
625 Maurice, S., Salvatore, M. and Wiens, R.C., (2017) Classification of igneous rocks analyzed by
626 ChemCam at Gale crater, Mars. Icarus, 288, pp.265-283.
627
628 Crowley, J. K., and D. R. Zimbleman (1997) Mapping hydrothermally altered rocks on Mount
629 Rainier, Washington, with Airborne Visible/Infrared Imaging Spectrometer (AVIRIS) data,
630 Geology, 25(6), 559-562.
631
632 Crowley, J. K., D. E. Williams, J. M. Hammarstrom, N. Piatak, I.-M. Chou, and J. C. Mars
633 (2003) Spectral reflectance properties (0.4-2.5 μm) of secondary Fe-oxide, Fe-hydroxide, and Fe-
634 sulphate-hydrate minerals associated with sulphide-bearing mine wastes, Geochemistry:
635 Exploration, Environment, Analysis, 3, 219-228.
636

637 Damer, B. et al. (2017) First and Last Outposts: The Origin and Preservation of Life in Terrestrial
638 and Martian Hydrothermal Field. The 3rd landing site workshop for the 2020 Mars Rover
639 mission, Pasadena, CA.
640
641 Danielsen, J. M. and J. L. Bishop (2018) Characterization of Jarosite-Bearing Outcrops at
642 Mawrth Vallis. 49th Lunar and Planetary Science Conference, Abstract #1804.
643
644 Dehouck, E., McLennan, S. M., Meslin, P. Y., and Cousin, A. (2014) Constraints on abundance,
645 composition, and nature of X-ray amorphous components of soils and rocks at Gale crater,
646 Mars. Journal of Geophysical Research: Planets, 119(12), 2640-2657.
647
648 De Rosa, M., Gambacorta, A., Millonig, G., and Bu'Lock, J. D. (1974) Convergent characters of
649 extremely thermophilic acidophilic bacteria. Experientia, 30(8), 866-868.
650
651 De Rosa, M., Gambacorta, A., and Bu'Lock, J. D. (1975) Extremely thermophilic acidophilic
652 bacteria convergent with Sulfolobus acidocaldarius. Microbiology, 86(1), 156-164.
653
654 Di Vito, M.A., Isaia, R., Orsi, G., Southon, J., De Vita, S., d'Antonio, M., Pappalardo, L., and
655 Piochi, M. (1999) Volcanism and deformation since 12,000 years at the Campi Flegrei caldera
656 (Italy). Journal of Volcanology and Geothermal Research, 91(2), 221-246.
657
658 Downs, R.T. and Hall-Wallace, M., (2003) The American Mineralogist Crystal Structure
659 Database. American Mineralogist, 88, 247-250.
660

661 Ehlmann, B. L. et al. (2009) Identification of hydrated silicate minerals on Mars using
662 MRO-CRISM: Geologic context near Nili Fossae and implications for aqueous alteration. Journal
663 of Geophysical Research: Planets, 114(E2).
664
665 Ehlmann, B. L. et al. (2011) Subsurface water and clay mineral formation during the early history
666 of Mars. Nature, 479, 53–60.
667
668 Ehlmann, B. L., Bish, D. L., Ruff, S. W., and Mustard, J. F. (2012) Mineralogy and chemistry of
669 altered Icelandic basalts: Application to clay mineral detection and understanding aqueous
670 environments on Mars. Journal of Geophysical Research: Planets, 117(E11).
671
672 Ehlmann, B. L. et al. (2013) Geochemical consequences of widespread clay mineral formation in
673 Mars' ancient crust. Space Science Reviews, 174(1–4), 329–364.
674
675 Ehlmann, B. L. et al. (2016) Discovery of alunite in Cross crater, Terra Sirenum, Mars: Evidence
676 for acidic, sulfurous waters. American Mineralogist, 101(7), 1527-1542.
677
678 Ehlmann, B. L. et al. (2017) Chemistry, mineralogy, and grain properties at Namib and High
679 dunes, Bagnold dune field, Gale crater, Mars: A synthesis of Curiosity rover observations.
680 Journal of Geophysical Research: Planets, 122(12), 2510-2543.
681
682 Elwood Madden, M.E., Bodnar R.J., and Rimstidt J.D. (2004) Jarosite as an indicator of water-
683 limited chemical weathering on Mars. Nature, 431, 821-823.
684

685 Farmer, J. D. (1996) Hydrothermal systems on Mars : an assessment of present evidence. Ciba
686 Foundation symposium 1996;202:273-95; discussion 295-9.
687
688 Farrand, W. H., Glotch, T. D., Rice Jr, J. W., Hurowitz, J. A., and Swayze, G. A. (2009)
689 Discovery of jarosite within the Mawrth Vallis region of Mars: Implications for the geologic
690 history of the region. Icarus, 204(2), 478-488.
691
692 Farrand, W. H., Glotch, T. D., and Horgan, B. (2014) Detection of copiapite in the northern
693 Mawrth Vallis region of Mars: Evidence of acid sulfate alteration. Icarus, 241, 346-357.
694
695 Ferrucci, F., Gaudiosi, G., Pino, N.A., Luongo, G., Hirn, A., Mirabile, L., (1989) Seismic
696 detection of a major Moho upheaval beneath the Campanian volcanic area, Naples, southern
697 Italy. Geophysical Research Letters, 16, 1317–1320.
698
699 Flahaut, J., et al. (2017a). Hydrothermal Alteration on Mars Compared to the Italian Solfatara. In
700 Lunar and Planetary Science Conference (Vol. 48).
701
702 Flahaut, J., Martinot, M., Bishop, J. L., Davies, G. R., and Potts, N. J. (2017b) Remote sensing
703 and in situ mineralogic survey of the Chilean salars: An analog to Mars evaporate deposits?
704 Icarus, 282, 152-173.
705
706 Fulignati, P. and Sbrana, A. (1998) Presence of native gold and tellurium in the active high-
707 sulfidation hydrothermal system of the La Fossa volcano (Vulcano, Italy). Journal of
708 Volcanology and Geothermal Research, 86(1-4), 187-198.

Gabriel, T. S. J. et al. (2018) Water abundance of dunes in Gale crater, Mars from active neutron experiments and implications for amorphous phases. Geophysical Research Letters, 45(23), 12-766.

Gražulis, S. et al., (2009) Crystallography Open Database–an open-access collection of crystal structures. Journal of Applied Crystallography, 42(4), 726-729.

Hausrath, E. M., D. C. Golden, R. V. Morris, D. G. Agresti, and D. W. Ming (2013) Acid sulfate alteration of fluorapatite, basaltic glass and olivine by hydrothermal vapors and fluids: Implications for fumarolic activity and secondary phosphate phases in sulfate-rich Paso Robles soil at Gusev Crater, Mars, Journal of Geophysical Research: Planets, 118, 1–13, doi:10.1029/2012JE004246.

Henke, K. (2009) Arsenic: environmental chemistry, health threats and waste treatment. John Wiley and Sons.

Huber, R., Huber, H., and Stetter, K. O. (2000a) Towards the ecology of hyperthermophiles: biotopes, new isolation strategies and novel metabolic properties. FEMS microbiology reviews, 24(5), 615-623.

Huber, R., Sacher, M., Vollmann, A., Huber, H., and Rose, D. (2000b) Respiration of arsenate and selenate by hyperthermophilic archaea. Systematic and applied microbiology, 23(3), 305-314.

Hynek, B. M., McCollom, T. M., Marcucci, E. C., Brugman, K., and Rogers, K. L. (2013) Assessment of environmental controls on acid-sulfate alteration at active volcanoes in Nicaragua: Applications to relic hydrothermal systems on Mars. Journal of Geophysical Research: Planets, 118(10), 2083-2104.

Isaia, R., Vitale, S., Di Giuseppe, M.G., Iannuzzi, E., Tramparulo, F.D.A., and Troiano, A., (2015) Stratigraphy, structure, and volcano-tectonic evolution of Solfatara maardiatreme (Campi Flegrei, Italy). Geological Society of America Bulletin, B31183-1.

Josset, J. L. et al. (2017) The Close-Up Imager onboard the ESA ExoMars Rover: objectives, description, operations, and science validation activities. Astrobiology, 17(6-7), 595-611.

Kabekkodu, S. N., Faber, J., and Fawcett, T., (2002) New Powder Diffraction File (PDF-4) in relational database format: advantages and data-mining capabilities. Acta Crystallographica Section B: Structural Science, 58(3), 333-337.

Klingelhöfer, G. R. D. S. et al. (2004) Jarosite and hematite at Meridiani Planum from Opportunity's Mössbauer spectrometer. Science, 306(5702), 1740-1745.

Kokaly, R.F., Clark, R.N., Swayze, G.A., Livo, K.E., Hoefen, T.M., Pearson, N.C., Wise, R.A., Benzel, W.M., Lowers, H.A., Driscoll, R.L., and Klein, A.J., (2017) USGS Spectral Library Version 7: U.S. Geological Survey Data Series 1035, 61 p., https://doi.org/10.3133/ds1035.

Korablev, O. I. et al. (2017) Infrared spectrometer for ExoMars: a mast-mounted instrument for the Rover. Astrobiology, 17(6-7), 542-564.

Lane, M. D., M. D. Dyar, and J. L. Bishop (2004) Spectroscopic evidence for hydrous iron sulfate in the Martian soil, Geophysical Research Letters, 31, L19702, doi:19710.11029/12004GL021231.

Lane, M. D., J. L. Bishop, M. D. Dyar, T. Hiroi, S. A. Mertzman, D. L. Bish, P. L. King, and A. D. Rogers (2015) Mid-infrared emission spectroscopy and visible/near-infrared reflectance spectroscopy of Fe-sulfate minerals, American Mineralogist, 100(1), 66-82, doi:10.2138/am-2015-4762.

Lopez-Reyes, G. et al. (2013) Analysis of the scientific capabilities of the ExoMars Raman Laser Spectrometer instrument. European Journal of Mineralogy, 25(5), 721-733.

Mayer, K., Scheu, B., Montanaro, C., Yilmaz, T. I., Isaia, R., Aßbichler, D., and Dingwell, D. B. (2016) Hydrothermal alteration of surficial rocks at Solfatara (Campi Flegrei): Petrophysical properties and implications for phreatic eruption processes. Journal of Volcanology and Geothermal Research, 320, 128-143.

Marcucci, E. C., Hynek, B. M., Kierein-Young, K. S., and Rogers, K. L. (2013) Visible-near-infrared reflectance spectroscopy of volcanic acid-sulfate alteration in Nicaragua: Analogs for early Mars. Journal of Geophysical Research: Planets, 118(10), 2213-2233.

McKeown, N. K., J. L. Bishop, J. Cuadros, S. Hillier, E. Amador, H. D. Makarewicz, M. Parente, and E. Silver (2011) Interpretation of reflectance spectra of clay mineral-silica mixtures: Implications for Martian clay mineralogy at Mawrth Vallis, Clays and Clay Mineral, 59(4), 400-415.

McSween, H. Y., Grove, T. L., and Wyatt, M. B. (2003) Constraints on the composition and petrogenesis of the Martian crust. Journal of Geophysical Research: Planets (1991–2012), 108(E12).

Michalski, J. R., P. B. Niles, J. Cuadros, and A. M. Baldridge (2013) Multiple working hypotheses for the formation of compositional stratigraphy on Mars: Insights from the Mawrth Vallis region, Icarus, 226(1), 816-840, doi:http://dx.doi.org/10.1016/j.icarus.2013.05.024.

Milliken, R. E. et al. (2008). Opaline silica in young deposits on Mars. Geology, 36(11), 847-850.

Morris, R.V. and Lauer Jr. H.V. (1990) Matrix effects for reflectivity spectra of dispersed nanophase (superparamagnetic) hematite with application to Martian spectral data. Journal of Geophysical Research, 95, 5101-5109.

Morris, R.V., Lauer Jr. H.V., Lawson C.A., Gibson Jr. E.K., Nace G.A., and Stewart C. (1985) Spectral and other physicochemical properties of submicron powders of hematite (a-Fe_2O_3), maghemite (g-Fe_2O_3), magnetite (Fe_3O_4), goethite (a-FeOOH), and lepidocrocite (g-FeOOH). Journal of Geophysical Research, 90, 3126-3144.

Morris, R. V., et al. (2006) Mössbauer mineralogy of rock, soil, and dust at Meridiani Planum, Mars: Opportunity's journey across sulfate-rich outcrop, basaltic sand and dust, and hematite lag deposits, Journal of Geophysical Research, 111(E12S15), doi:10.1029/2006JE002791.

Murchie, S. et al., (2007) Compact reconnaissance Imaging Spectrometer for Mars (CRISM) on Mars Reconnaissance Orbiter (MRO). Journal of Geophysical Research, 112 (E5), E05S03. http://dx.doi.org/10.1029/2006JE002682.

Murchie, S. L. et al. (2009) A synthesis of Martian aqueous mineralogy after 1 Mars year of observations from the Mars Reconnaissance Orbiter. Journal of Geophysical Research, 114, E00D06, doi:10.1029/2009JE003342.

Mustard, J. F. et al. (2008) Hydrated silicate minerals on Mars observed by the Mars Reconnaissance Orbiter CRISM instrument. Nature, 454(7202), 305.

Nisbet, E. G. and Sleep, N. H. (2001) The habitat and nature of early life. Nature, 409(6823), 1083-1091.

Pappalardo L, Piochi M, D'Antonio M, Civetta L, Petrini R (2002) Evidence for multi-stage magmatic evolution during the past 60 kyr at Campi Flegrei (Italy) deduced from Sr, Nd and Pb isotope data. Journal of Petrology, 43:1415–1434. doi:10.1093/petrology/43.8.1415.

Piochi, M., C. R. J. Kilburn, M. A. Di Vito, A. Mormone, A. Tramelli, C. Troise, and G. De Natale (2014) The volcanic and geothermally active Campi Flegrei caldera: An integrated

multidisciplinary image of its buried structure, International Journal of Earth Sciences, 103(2), 401–421, doi:10.1007/s00531-013-0972-7.

Piochi, M., Mormone, A., Balassone, G., Strauss, H., Troise, C., and De Natale, G., (2015) Native sulfur, sulfates and sulfides from the active Campi Flegrei volcano (southern Italy): Genetic environments and degassing dynamics revealed by mineralogy and isotope geochemistry. Journal of Volcanology and Geothermal Research, 304, 180-193.

Rampe, E. B. et al. (2018) Sand mineralogy within the Bagnold Dunes, Gale crater, as observed in situ and from orbit. Geophysical Research Letters, 45(18), 9488-9497.

Rosi, M., and Sbrana A. (1987) Phlegrean Fields: Petrography, Quad. Ricerca Sci., 114, 60–79.

Rosi, M., Sbrana, A., Principe, C., (1983) The Phlegrean Fields: structural evolution, volcanic history and eruptive mechanism. Journal of Volcanology and Geothermal Research, 17, 249–273.

Rye, R.O. (2005) A review of the stable-isotope geochemistry of sulfate minerals in selected igneous environments and related hydrothermal systems. Chemical Geology, 215(1), 5-36.

Ruff, S. W. et al. (2011) Characteristics, distribution, origin, and significance of opaline silica observed by the Spirit rover in Gusev crater, Mars. Journal of Geophysical Research: Planets, 116(E7).

852 Ruff, S. W., Niles, P. B., Alfano, F., and Clarke, A. B. (2014) Evidence for a Noachian-aged
853 ephemeral lake in Gusev crater, Mars. Geology, 42(4), 359-362.
854
855 Ruff, S. W. and Farmer, J. D. (2016) Silica deposits on Mars with features resembling hot spring
856 biosignatures at El Tatio in Chile. Nature communications, 7, 13554.
857
858 Rull, F. et al. (2017) The Raman laser spectrometer for the ExoMars Rover mission to Mars.
859 Astrobiology, 17(6-7), 627-654.
860
861 Sautter, V. et al. (2015) In situ evidence for continental crust on early Mars. Nature Geoscience,
862 8(8), 605-609.
863
864 Schiffman, P., Zierenberg, R., Marks, N., Bishop, J. L., and Dyar, M. D. (2006) Acid-fog
865 deposition at Kilauea volcano: A possible mechanism for the formation of siliceous-sulfate rock
866 coatings on Mars. Geology, 34(11), 921-924.
867
868 Seelos, K. D., Arvidson, R. E., Jolliff, B. L., Chemtob, S. M., Morris, R. V., Ming, D. W., and
869 Swayze, G. A. (2010) Silica in a Mars analog environment: Ka'u Desert, Kilauea Volcano,
870 Hawaii. Journal of Geophysical Research: Planets, 115(E4).
871
872 Sessa, A. M., J. J. Wray, J. L. Bishop (2018) Discovery of Alunite in Candidate ExoMars
873 Landing Site, Mawrth Vallis: Evidence for Localized Evaporative Environments, 49th Lunar and
874 Planetary Science Conference, Abstract #2983.
875

876 Sgavetti, M. et al. (2009) Two geologic systems providing terrestrial analogues for the
877 exploration of sulfate deposits on Mars: Initial spectral characterization. Planetary and Space
878 Science, 57(5), 614-627.
879
880 Shock, E. L. (1996) Hydrothermal systems as environments for the emergence of life. Ciba
881 Foundation symposium 202(202):40-52; discussion 52-60.
882
883 Skok, J. R., Mustard, J. F., Ehlmann, B. L., Milliken, R. E., and Murchie, S. L. (2010) Silica
884 deposits in the Nili Patera caldera on the Syrtis Major volcanic complex on Mars. Nature
885 Geoscience, 3(12), 838.
886
887 Sobron, P., J. L. Bishop, D. F. Blake, B. Chen, and F. Rull (2014) Natural Fe-bearing oxides and
888 sulfates from the Rio Tinto Mars analogue – Critical assessment of VNIR reflectance
889 spectroscopy, laser Raman spectroscopy, and XRD as mineral identification tools, American
890 Mineralogist, 99(7), 1199-1205.
891
892 Squyres, S. W. et al. (2008) Detection of silica-rich deposits on Mars. Science, 320(5879), 1063-
893 1067.
894
895 Sun, V.Z. and Milliken R.E. (2018) Distinct Geologic Settings of Opal-A and More Crystalline
896 Hydrated Silica on Mars. Geophysical Research Letters, 45, 10,221-10,228.
897

Swayze, G. A. et al. (2008) Discovery of the acid-sulfate mineral alunite in Terra Sirenum, Mars, using MRO CRISM: Possible evidence for acid-saline lacustrine deposits?. In AGU Fall Meeting Abstracts.

Tedesco, D. and Sabroux, J. C. (1987) The determination of deep temperatures by means of the CO-CO 2-H 2-H 2 O geothermometer: an example using fumaroles in the Campi Flegrei, Italy. Bulletin of volcanology, 49(1), 381-387.

Tedesco, D., Pece, R., and Sabroux, J. C. (1988) No evidence of a new magmatic gas contribution to the Solfatara volcanic gases, during the Bradyseismic crisis at Campi Flegrei (Italy). Geophysical Research Letters, 15(12), 1441-1444.

Tedesco, D. (1994) Chemical and isotopic gas emissions at Campi Flegrei: Evidence for an aborted period of unrest. Journal of Geophysical Research, 15623-15631.

Torrente, M. M., Milia, A., Bellucci, F., and Rolandi, G. (2010) Extensional tectonics in the Campania Volcanic Zone (eastern Tyrrhenian Sea, Italy): new insights into the relationship between faulting and ignimbrite eruptions. Italian journal of geosciences, 129(2), 297-315.

Thollot, P. et al. (2012) Most Mars minerals in a nutshell: Various alteration phases formed in a single environment in Noctis Labyrinthus. Journal of Geophysical Research: Planets, 117(E11).

Valentino, G. M., Cortecci, G., Franco, E., and Stanzione, D. (1999) Chemical and isotopic compositions of minerals and waters from the Campi Flegrei volcanic system, Naples, Italy. Journal of Volcanology and Geothermal Research, 91(2), 329-344.

Viviano, C. E., Moersch, J. E., and McSween, H. Y. (2013) Implications for early hydrothermal environments on Mars through the spectral evidence for carbonation and chloritization reactions in the Nili Fossae region. Journal of Geophysical Research: Planets, 118(9), 1858-1872.

Viviano-Beck, C. E., et al. (2014) Revised CRISM spectral parameters and summary products based on the currently detected mineral diversity on Mars, Journal of Geophysical Research: Planets, 119, 1403–1431, doi:10.1002/2014JE004627.

Viviano-Beck, C. E. et al. (2015) MRO CRISM Type Spectra Library, NASA Planetary Data System, http://crismtypespectra.rsl.wustl.edu.

Weitz, C.M., Bishop J.L., Thollot P., Mangold N., and Roach L.H. (2011) Diverse mineralogies in two troughs of Noctis Labyrinthus, Mars. Geology, 39, 899-902, doi: 10.1130/G32045.1.

Weitz, C. M., J. L. Bishop, and J. A. Grant (2013) Gypsum, opal, and fluvial channels within a trough of Noctis Labyrinthus, Mars: Implications for aqueous activity during the Late Hesperian to Early Amazonian, Planetary and Space Science, 87, 130-145.

942 Weitz, C. M., J. L. Bishop, L. L. Baker, and D. C. Berman (2014) Fresh exposures of hydrous Fe-
943 bearing amorphous silicates on Mars. Geophysical Research Letters, 41(24), 8744–8751,
944 doi:10.1002/2014GL062065.
945
946 Wiens, R. C., et al. (2016) The SuperCam remote sensing instrument suite for Mars 2020. In 47th
947 Lunar and Planetary Science Conference, abstract #1322.
948
949 Wray, J. J., et al. (2011) Columbus crater and other possible groundwater-fed paleolakes of Terra
950 Sirenum, Mars. Journal of Geophysical Research: Planets, 116(E1).
951
952 Yen, A. S. et al. (2017) Multiple stages of aqueous alteration along fractures in mudstone and
953 sandstone strata in Gale Crater, Mars. Earth and Planetary Science Letters, 471, 186-198.
954
955 Zillig, W., Stetter, K. O., Wunderl, S., Schulz, W., Priess, H., and Scholz, I. (1980) The
956 Sulfolobus-"Caldariella" group: taxonomy on the basis of the structure of DNA-dependent RNA
957 polymerases. Archives of Microbiology, 125(3), 259-269.
958
959 Zimbelman, D.R., Rye, R.O., and Breit, G.N., (2005) Origin of secondary sulfate minerals on
960 active andesitic stratovolcanoes. Chemical Geology, 215(1), 37-60.
961
962
963
964
965

This is a preprint, the final version is subject to change, of the American Mineralogist (MSA)
Cite as Authors (Year) Title. American Mineralogist, in press.
DOI: https://doi.org/10.2138/am-2019-6899

966 **Figure captions**

967 Figure 1: a) Location of the study area in Italy. b) View of the Campanian plain and the three
968 volcanoes from the bay of Naples: Vesuvio (V), Campi Flegrei (CF) and Ischia (I). c) Close-up
969 view on the Solfatara volcanic crater. Sampling sites are indicated by green stars. Faults and ring
970 faults from Isaia et al. (2015) are overlain in transparency, and represented by black and red lines
971 respectively (Background: ArcGIS world imagery maps, Sources: Esri, DigitalGlobe, GeoEye,
972 Earthstar Geographics, CNES/Airbus DS, USDA, USGS, AeroGRID, IGN, and the GIS User
973 Community).

974

975 Figure 2: Field impressions at the different sampling sites (See locations on figure 1).

976

977 Figure 3: VNIR reflectance spectra of selected samples that represent the types of spectral
978 features observed (thick lines). a) Altered walls at L2 and L6, b) mudpot sediments from L1,
979 c) deposits from the L6 90°C vent, d) deposits from the L4 160°C vent. Reflectance spectra of
980 minerals likely present, from the Bishop collection and the USGS spectral library, are given for
981 comparison (dotted lines). Vertical bars were placed at key wavelengths to facilitate comparison
982 of the absorption features.

983

984 Figure 4: Raman spectra of selected samples that represent the types of spectral features
985 observed. a) Altered walls at L6, b) mudpots sediments from L1, c) deposits at the L4 160°C
986 vent). RUFF reference library spectra of the minerals commonly identified in the samples are
987 given for comparison (dotted lines). Vertical bars were placed at key wavelengths to facilitate
988 comparison of the Raman peaks.

989

Figure 5: VNIR field spectra of alunite and jarosite in rock coatings, which are occurring within the same outcrops at the Solfatara crater, are compared with the spectra of terrestrial references and Mawrth Vallis (MW) Mars locations from the Bishop collection (Bishop et al., 2004b, 2018; Bishop and Murad, 2005) and the Viviano-Beck et al. (2014) type spectra marked by V.

Figure 6: Mars examples of alunite, jarosite and silica detections. a) Silica-rich deposits (magenta arrows) identified around the Nili Patera volcanic cone by Skok et al. (2010). The opal_index parameters map (in rainbow, stretched values 0.001-0.1) using the index of Thollot et al. (2012) on CRISM FRT00010628 is overlain in transparency over CTX image B05_011459_1891_XI_09N292W. b) Sporadic alunite (yellow arrows) and jarosite (orange arrows) detections were made within the clay-rich units of Mawrth Vallis (locations from Danielson and Bishop, 2018; Bishop et al., 2018; Sessa et al., 2018). CRISM observation FRT00003BFB is displayed in false color (default RGB, R=2.5361 μm, G=1.3358 μm, B= 0.7749 μm) over CTX image P03_002074_2027_XI_22N018W. c) Alunite is detected together with kaolinite along the walls of the 65 km diameter Cross Crater (Ehlmann et al., 2018). RGB composite of CRISM observations FRT000137C2, FRT0000D24B, FRT0000CC44, FRT0000B252, FRT0000987B are overlain over CTX images D16_033383_1496_XN_30S157W, P16_007446_1477_XN_32S157W, P19_008448_1493_XN_30S158W, P20_009028_1495_XI_30S157W, P15_006945_1494_XN_30S158W. This RGB composite with the summary parameters R=BD2200 (Thollot et al., 2012), G=Kaol-index (Thollot et al., 2012), B= SINDEX2 (Viviano-Beck et al., 2014) was chosen to highlight putative alunite detections in purple, and kaolinite detections in yellow (mixed detections appear in white). d) CRISM VNIR spectra of selected Mars mineral detections are compared with library references (Mars spectra: CRISM alunite and

This is a preprint, the final version is subject to change, of the American Mineralogist (MSA)
Cite as Authors (Year) Title. American Mineralogist, in press.
DOI: https://doi.org/10.2138/am-2019-6899

jarosite spectra from Viviano-Beck et al. (2014, 2015) and Bishop et al. (2018), Silica spectra from CRISM FRT00010628 (average of 3x3 pixels). Reference spectra: Alunite GDS83, Jarosite GDS99 and Opal TM8896 from the USGS spectral library).

Tables

Table 1: List of sampling sites and collected samples.

site	Latitude	Longitude	Type	Description of samples
L1	40.8270	14.1393	mudpot at 33°C, pH = 1.5	R1: white/brown deposits outside the pool. Polygons on a 20 cm scale R2: yellowish/brown deposits outside the pool R3: hard cemented deposits on the pool ramparts (Z1= at surface, Z2 = at a 5cm depth) R4: Light gray, wet sediments from the pool
L2	40.8303	14.1393	weathered wall	R1: Yellow coatings R2: Orange coatings R3 : Red coatings
L3	40.8304	14.1395	weathered wall	R1: white ignimbrite / ashy layer from the crater wall R2: white ignimbrite / pumice from the crater wall R3: yellowish ignimbrite / ashy layer from the crater wall
L4	40.8271	14.1420	fumarolic vent at 160°C	R1: colorful rock lying on the vent (white, yellow, orange, dark and burgundy coatings) R2: colorful rock lying on the vent (yellow and orange coatings)
L5	40.8255	14.1393	fumarolic vent at 90°C	R1 : white material within the vent R2: yellow material (sulfur needles) within the vent R3: friable/ altered, white/beige rocks around the vent R4: friable/ altered rocks with subtle turquoise tones around the vent
L6	40.8295	14.1407	fumarolic vent	R1: White pyroclastic deposits in the crater wall

This is a preprint, the final version is subject to change, of the American Mineralogist (MSA)
Cite as Authors (Year) Title. American Mineralogist, in press.
DOI: https://doi.org/10.2138/am-2019-6899

			at 90°C + weathered wall	R2: Beige pyroclastic deposits in the crater wall R3: Orange/Brown coatings on the crater wall R4: Yellow coatings on the crater wall R5: Dark red coatings on the crater wall R6: Sea green/turquoise coatings on the crater wall R7: Biology - green layer of algae, possibly Cyanidium caldarium R8: White coatings R9: Yellow sulfur crystals R10: Rock with colorful coatings R11: Yellow sulfur crystals from within a vent R12: White fibrous deposits from within a vent R13: White nodular material from within a vent R14: Orange nodular material from within a vent R15: Orange/brown puffy material from within/around a vent R16: White puffy material from within/around a vent R17: White/beige nodular material around the vent R18: White nodular material around the vent R19: Orange/brown ridged/puffy material around the vent R20: White/orange deposits from within a second vent R21: Orange/dark brown deposits from within a second vent
L7	40.8290	14.1405	dry mudpot	R1: brown deposits, polygons on a 10 cm scale.

1022

1023

This is a preprint, the final version is subject to change, of the American Mineralogist (MSA)
Cite as Authors (Year) Title. American Mineralogist, in press.
DOI: https://doi.org/10.2138/am-2019-6899

1024

1025 Table 2: Bulk composition of selected crater wall samples that appeared relatively unaltered. All
1026 values are given in wt%; D. L.= Detection Limit. Major oxides have been renormalized to 100%
1027 to exclude the loss on ignition. This Ignition loss (as measured by ICP-OES, including S) and the
1028 S content (as measured separately, by a C-S analyzer) are given for information. The Chemical
1029 Index of Alteration (CIA) is calculated using the equation of Nesbitt and Young (1982): CIA =
1030 (Al2O3) x 100 x $(Al2O3 + CaO + Na2O + K2O)^{-1}$. CIA values fall within the same range (60-80)
1031 of Mayer et al. (2016) who noticed that the Solfatara sample density decreases (porosity
1032 increases) with increasing degree of alteration.

Sample ID	SiO_2	Al_2O_3	Fe_2O_3	MnO	MgO	CaO	Na_2O	K_2O	TiO_2	P_2O_5	Total major oxides	Ignition loss	S	CIA
L5R4	97.56	0.72	0.08	<D.L.	<D.L.	0.05	0.09	0.22	1.27	<D.L.	100	**16.52**	**1.36**	66.30
L3R1	97.03	1.19	0.14	<D.L.	0.06	0.08	0.14	0.11	1.26	<D.L.	100	**6.41**	**0.35**	78.37
L6R1	97.16	1.54	0.13	<D.L.	0.05	0.05	0.12	0.10	0.86	<D.L.	100	**12.37**	**0.46**	84.95

1033

1034

1035

Table 3: Summary of XRD detections for selected samples. For the DOC (degree of crystallinity) values, the -, +, ++ and +++ symbols indicate the following ranges of values, respectively : <30%, >30%, >50%, >70%. For mineral abundances within the crystalline phases, the -, +, ++ and +++ symbols indicate the following ranges of values, respectively : present but <10%, >10%, >40%, >70%. Gray lines indicate samples with a lower amount of crystalline phases (<60%). Sulf= Sulfur, Cal = calcite, Ana = Anatase, San= sanidine, Al= alunite, Jar = jarosite, Alg = alunogen, Alum = alum-K, Mer = mercallite, Gol =Goldichite, Coq = coquimbite, Pick = pickeringite, Mag =magnesite, Cam= caminite, Fer = ferrhydrite, Yav = Yavapaiite, Mil = millosevichite, Mic= mica, Tam = tamarugite.

Sample ID	DOC	Sulf	Cal	Ana	San	Al	Jar	Alg	Alum	Mer	Gol	Coq	Pick	Mag	Cam	Fer	Yav	Mil	Mic	Tam
L5R1	-	+++	-	-										-						
L5R3	++	+++	-																	
L5R4	-		+	++																
L3R1	-		+	+++																
L6R1	-		++	++																
L6R3	+++				+++	-	-												-	
L6R4	++					+++	-	-							-					
L6R5	+++				+++		-												-	
L1R2Z1	+++					-		++	+				+							
L1R3Z1	++	++				+														
L1R3Z2	+	+++		-		+														
L1R4	++	++				++														
L6R11	+++	+++						-	-											
L6R12	+++							++	+	-							-			
L6R13	+++							++	+		+									
L6R14	++					+++		+	+		-									
L6R15	+++					-		++	+		-	-								-
L6R16	+++	-				+		++	+											
L6R17	+++					-		+++	+		-							-		
L6R18	+++					-		+++	-	-										
L6R19	+++					+		++			+	-								

This is a preprint, the final version is subject to change, of the American Mineralogist (MSA)
Cite as Authors (Year) Title. American Mineralogist, in press.
DOI: https://doi.org/10.2138/am-2019-6899

L6R20	++	-				+		+++		-					-				
L6R21	+++	-				+		+	++										

Table 4 : Bulk composition of the mudpot samples. Major oxides (renormalized, see Table 2 for more information), ignition loss and S values are given in wt%, As and Sb and given in ppm. D. L.= Detection Limit.

Sample ID	SiO_2	Al_2O_3	Fe_2O_3	MnO	MgO	CaO	Na_2O	K_2O	TiO_2	P_2O_5	Total major oxides	Ignition loss	S	As	Sb
L1R3Z1	92.08	5.34	0.19	<D.L.	<D.L.	0.07	0.15	1.28	0.88	<D.L.	100	42.31	23.62	47.54	27.12
L1R4	84.95	9.96	0.46	<D.L.	<D.L.	0.13	0.24	2.70	1.37	0.18	100	44.17	18.56	53.48	13.62

Table 5: Main mineralogical assemblages at the various crater locations, as determined from the three main instrument techniques described here. Asterisks (*) indicate locations where XRD data show a relatively high proportion (> 50%) of amorphous material in some samples. Hem = Hematite, Cin = Cinnabar, Real = Realgar, Orp = Orpiment, Cop = Copiapite.

	XRD	Raman	VNIR
Mudpots at L1, L7	Sulf, Al, Alg, Alum, pick*	Sulf, pick/sulfates, Opal	Opal (+ Al-clays at L7)
Relatively unaltered walls at L5 and L6 (R1-2)	Sulf, Cal, Ana*	-	Opal
Colorful alteration at L2, L3 and L6 (R3-10)	San, Al, Jar, (Cam, Mic, Alg)	San, Al, Jar	Al, Jar, hem, opal
Sublimates at L4	-	As species	Cin, Real, Orp, Al, dehydrated opal
Sublimates at L6 (R11-21)	Alg, Al, Alum, Gol, Mer, Coq,(Mil, Yav, Tam)	-	water saturated component (Alg?), cop, coq, hem

This is a preprint, the final version is subject to change, of the American Mineralogist (MSA)
Cite as Authors (Year) Title. American Mineralogist, in press.
DOI: https://doi.org/10.2138/am-2019-6899

Figure 1

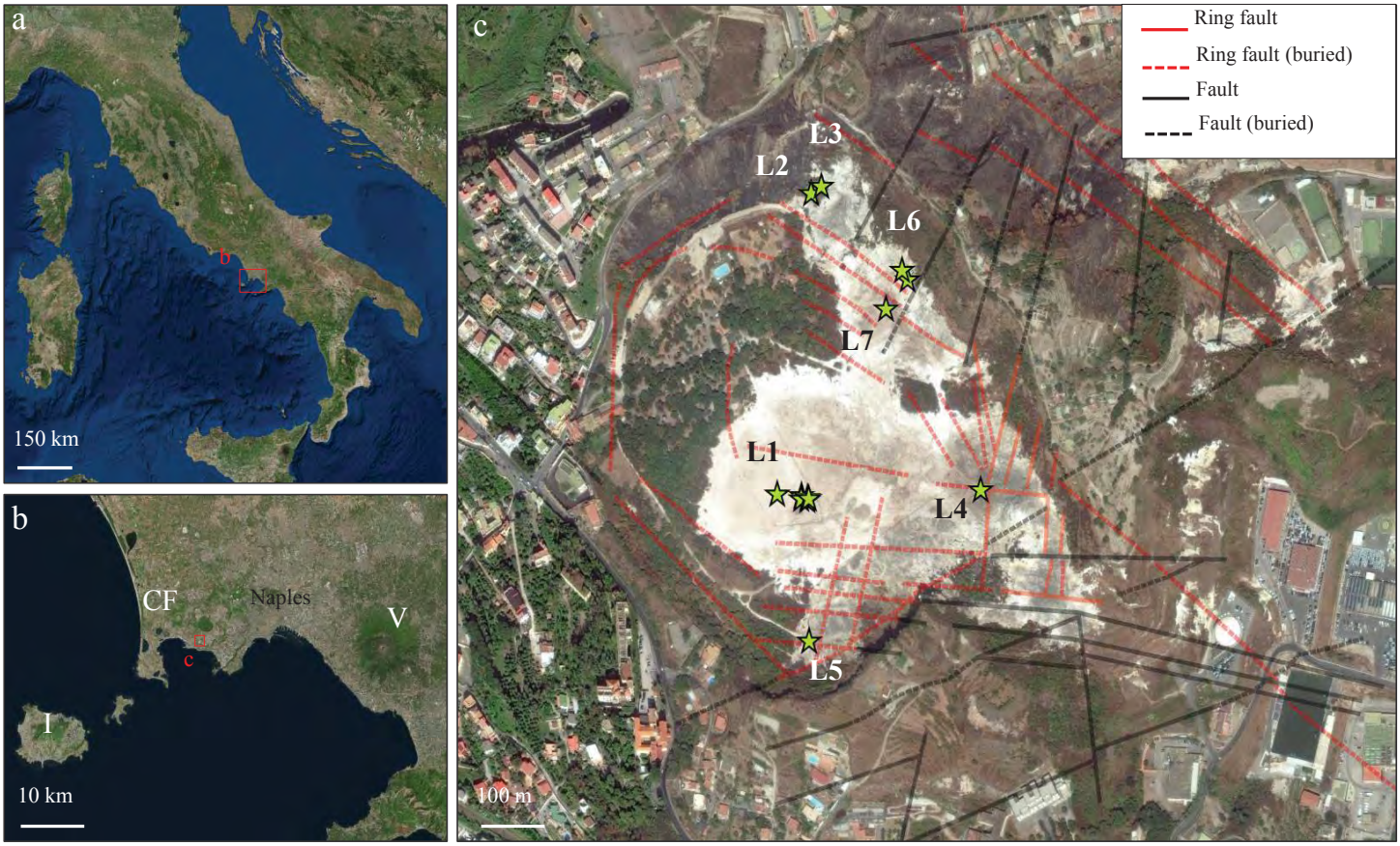

This is a preprint, the final version is subject to change, of the American Mineralogist (MSA)
Cite as Authors (Year) Title. American Mineralogist, in press.
DOI: https://doi.org/10.2138/am-2019-6899

Figure 2

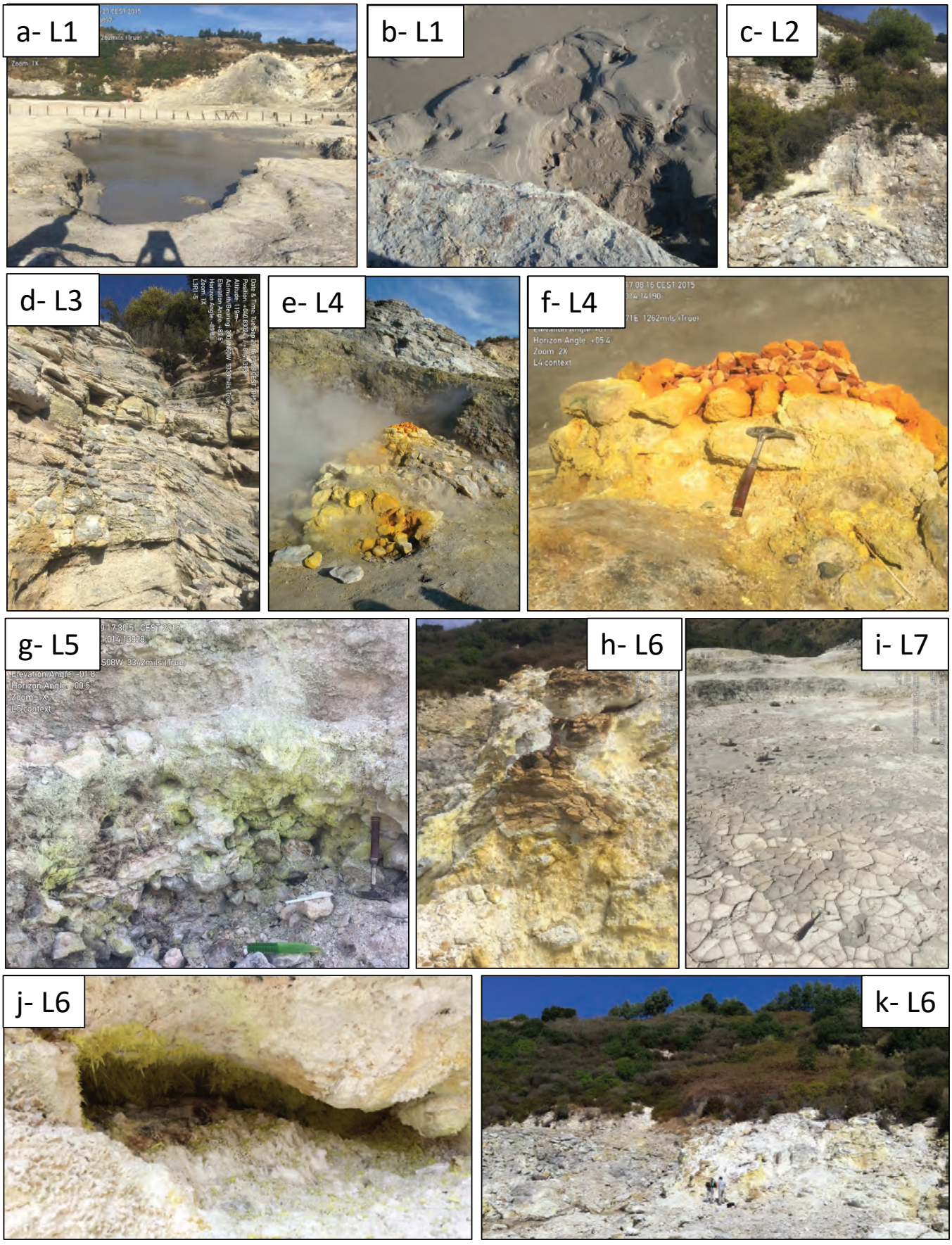

This is a preprint, the final version is subject to change, of the American Mineralogist (MSA)
Cite as Authors (Year) Title. American Mineralogist, in press.
DOI: https://doi.org/10.2138/am-2019-6899

Figure 3

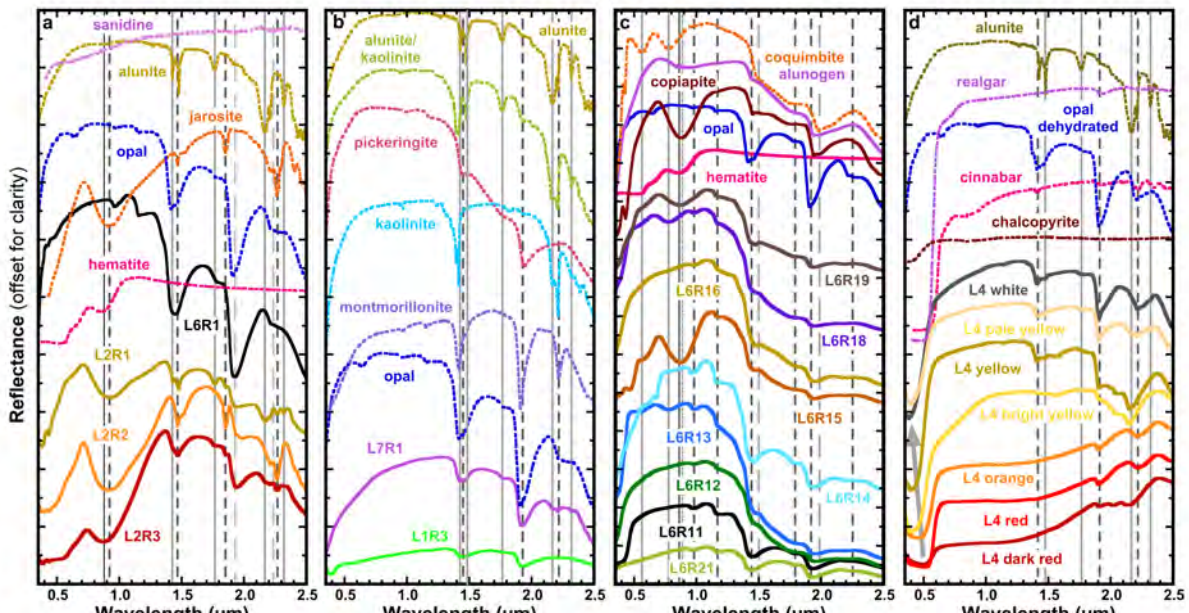

This is a preprint, the final version is subject to change, of the American Mineralogist (MSA)
Cite as Authors (Year) Title. American Mineralogist, in press.
DOI: https://doi.org/10.2138/am-2019-6899

Figure 4

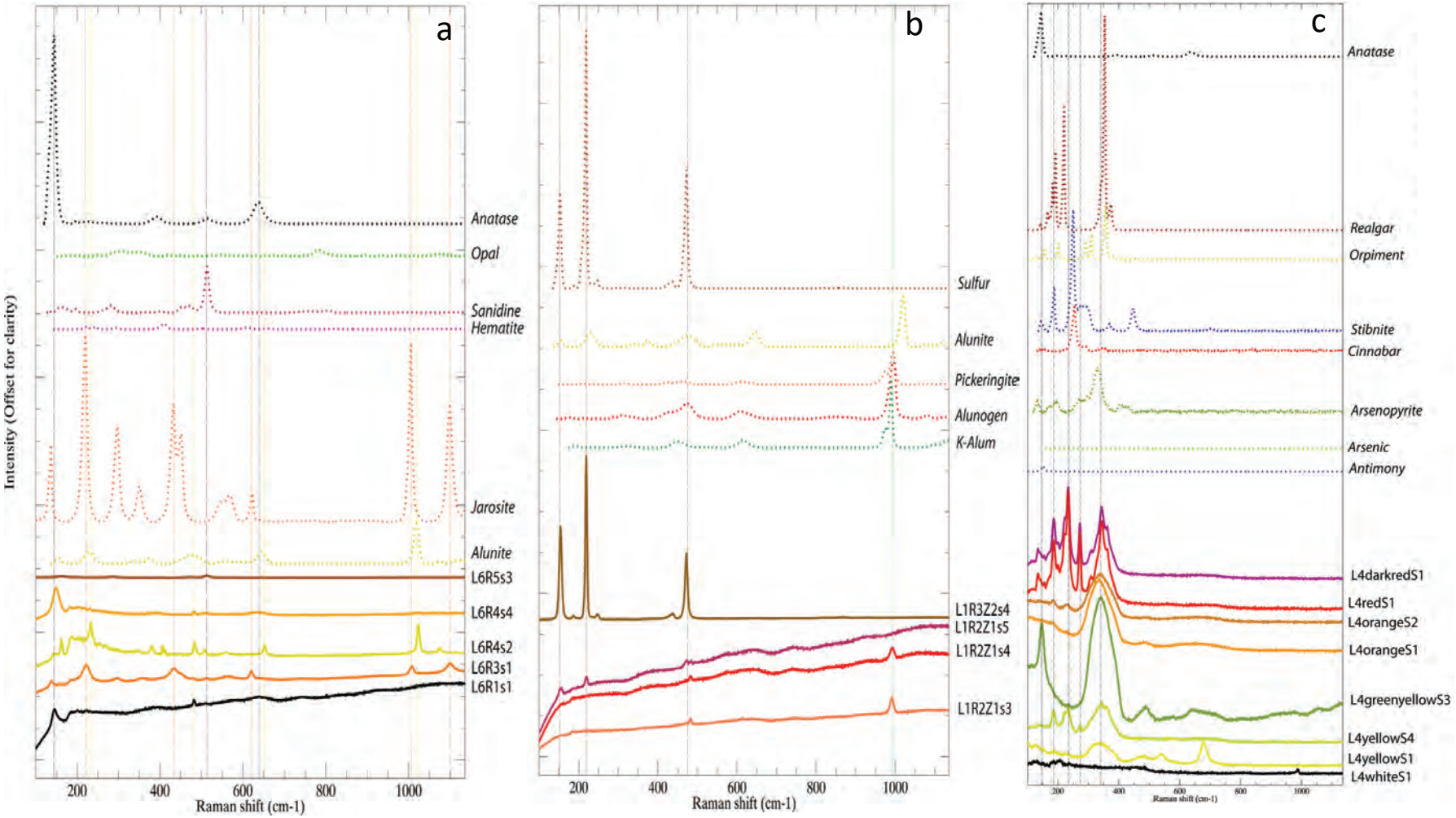

This is a preprint, the final version is subject to change, of the American Mineralogist (MSA)
Cite as Authors (Year) Title. American Mineralogist, in press.
DOI: https://doi.org/10.2138/am-2019-6899

Figure 5

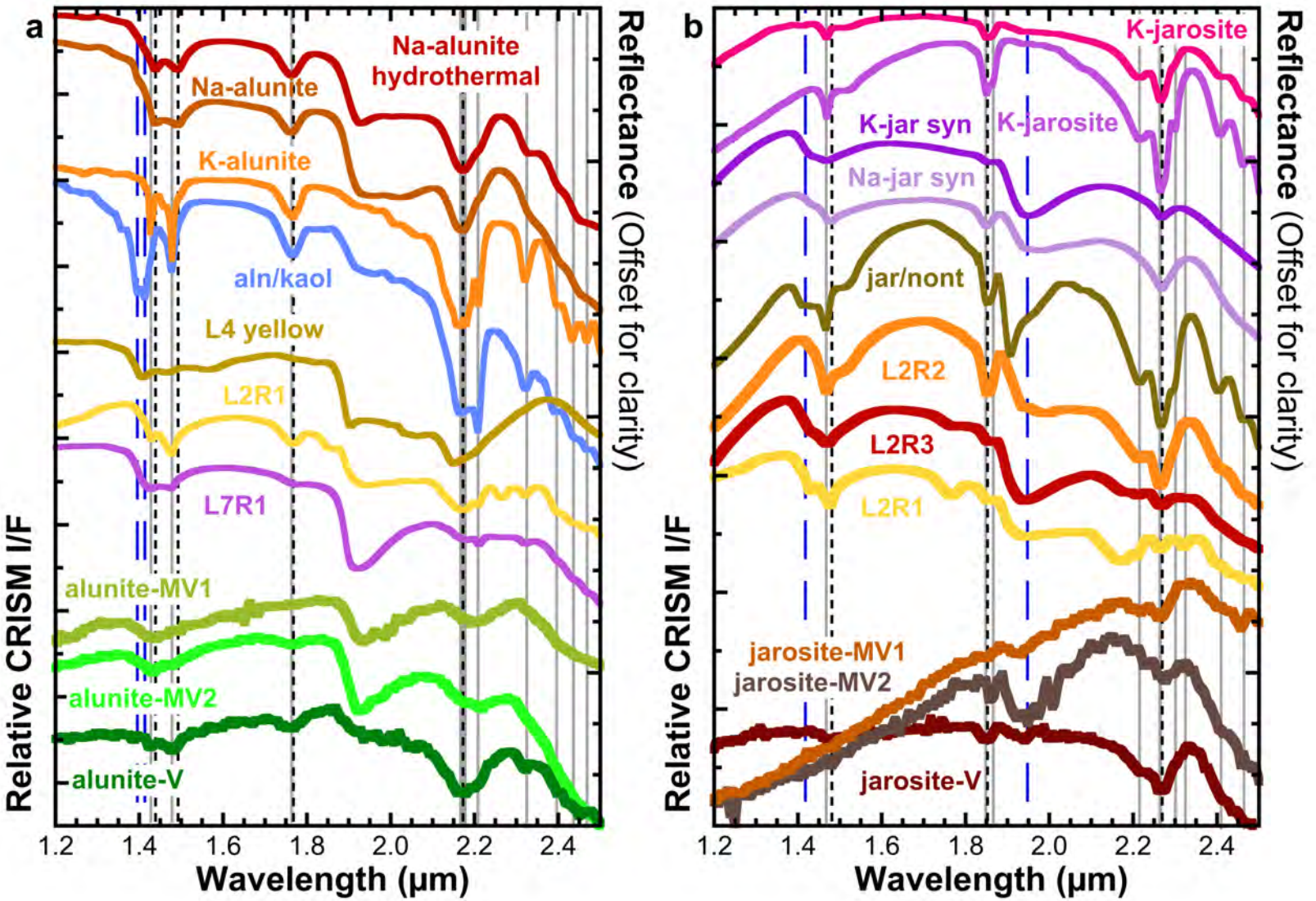

This is a preprint, the final version is subject to change, of the American Mineralogist (MSA)
Cite as Authors (Year) Title. American Mineralogist, in press.
DOI: https://doi.org/10.2138/am-2019-6899

Figure 6